Lattice Boltzmann modeling and simulation of velocity and concentration slip effects on the catalytic reaction rate of strongly nonequimolar reactions in microflows

Meysam Khatoonabadi [*]
Paul Scherrer Institute, Laboratory for Scientific Computing and Modeling, Division Scientific Computing, Theory, and Data, CH-5232 Villigen PSI, Switzerland

Nikolaos I. Prasianakis [†]
Paul Scherrer Institute, Waste Management Laboratory, Nuclear Energy and Safety Division, CH-5232 Villigen-PSI, Switzerland

John Mantzaras [‡]
Paul Scherrer Institute, Laboratory for Scientific Computing and Modeling, Division Scientific Computing, Theory, and Data, CH–5232 Villigen PSI, Switzerland

(Received 19 September 2022; accepted 29 November 2022; published 21 December 2022)

A lattice Boltzmann (LB) interfacial gas-solid three-dimensional model is developed for isothermal multicomponent flows with strongly nonequimolar catalytic reactions, further accounting for the presence of velocity slips and concentration jumps. The model includes diffusion coefficients of all reactive species in the calculation of the catalytic reaction rates as well as an updated velocity at the reactive boundary node. Lattice Boltzmann simulations are performed in a catalytic channel-flow geometry under a wide range of Knudsen (Kn) and surface Damköhler (Da_s) numbers. Comparisons with simulations from a computational fluid dynamics (CFD) Navier-Stokes solver show good agreement in the continuum regime (Kn < 0.01) in terms of flow velocity and reactive species distributions, while comparisons with direct simulation Monte Carlo results from the literature attest to the model's applicability in capturing the correct slip velocity at Kn as high as 0.1, even with a significantly reduced number of grid points ($N = 10$) in the cross-flow direction. Theoretical and numerical results demonstrate that the term $Da_s \times Kn \times A_2$ (where A_2 is a function of the mass accommodation coefficient) determines the significance of the concentration jump on the catalytic reaction rate. The developed model is applicable for many catalytic microflow systems with complex geometries (such as reactors with porous networks) and large velocity/concentration slips (such as catalytic microthrusters for space applications).

DOI: 10.1103/PhysRevE.106.065305

I. INTRODUCTION

Microscale gas flows are of main interest for many practical systems that are used for extracting biological samples, cooling integrated circuits, controlling aerodynamic characteristics, and facilitating high-efficiency microreactors [1–3]. One of the fluid phenomena observed in microdevices is slip flow. Slip flow occurs due to nonequilibrium processes at the molecular level, and it manifests itself with velocity, concentration, and temperature slips at the gas-solid interfaces.

For the particular case of isothermal microflows, a proper numerical model requires accurate estimation of velocity and concentration slips at the solid-gas boundary. The nondimensional Knudsen number (Kn), defined as the ratio of the gas mean free path (λ) to a characteristic geometrical length (l), determines the importance of velocity and concentration slips in small-scale isothermal fluid flow simulations. Based on the Knudsen number, the flow regimes are categorized as continuum (Kn < 0.01), slip ($0.01 <$ Kn < 0.1), transitional ($0.1 <$ Kn < 10), and free molecular ($10 <$ Kn). For the simulation of flows over catalytic surfaces, in particular, it is essential to accurately model both the bulk flow and the reacting solid boundary. Continuum approaches based on the Navier-Stokes equations are still valid up to Kn $= 0.1$, provided that a correct slip boundary condition is employed at the solid walls [3].

Within the lattice Boltzmann (LB) framework, the accuracy of the bounce-back boundary condition with different implementation approaches in the continuum regime has been thoroughly discussed by Kruger *et al.* [4]. The presence of a numerical slip velocity (spurious slip velocity) has been demonstrated when using different relaxation times [4]. This issue mostly shows up in the simulation of channel flows with a reduced number of grid points; it has been described either as the dependency of the numerical slip error on relaxation time (τ), or as the variation of the exact location of the wall at different relaxation times [4]. In other words, while the effect of slip is captured in a qualitative way, as predicted in kinetic theory, quantitatively it leads to an overestimated slip velocity that introduces significant deviations in the solution [5]. One common method to overcome the spurious slip velocity is

[*]seyyed-meysam.khatoonabadi@psi.ch
[†]nikolaos.prasianakis@psi.ch
[‡]Corresponding author: ioannis.mantzaras@psi.ch

by tuning the relaxation time such that no-slip velocity is achieved through either multi-relaxation-time approaches or an adjustable single relaxation time [5–8]. This approach is widely utilized in complex geometries such as porous media, where it is not always possible to refine the grid everywhere in the domain, and the Knudsen number can be very small ($\mathrm{Kn} \ll 0.01$). It results in a specific value for the relaxation time, for which the spurious numerical slip vanishes [5,9–12]. Chai *et al.* [13] used a modified relaxation time based on the flow Knudsen number to incorporate the effect of velocity slip at the solid boundary. However, this modeling becomes complicated for multicomponent gas mixture flows with slip velocities, whereby the relaxation times are directly related to physical parameters (e.g., viscosity and diffusivity of a given species) that may additionally vary spatially and temporally. Moreover, tuning (mostly reducing) the relaxation time leads to a decreasing time step, and hence to increased simulation wall clock time. Consequently, this is not the preferred approach for multicomponent mixture simulations with appreciably high Knudsen numbers ($\mathrm{Kn} > 0.01$) and a reduced number of grid points.

Several LB models have been proposed for the slip velocity, which can be divided into three main categories. In the first group, the viscosity (or relaxation time) is tuned in order to recover the correct slip velocity. Similar approaches have defined an effective viscosity in the bulk flow of the whole simulation domain [5,14], while others introduced an equation to modify the viscosity as a function of distance to the nearest solid wall [15–18]. The latter approach is also common in numerical methods other than LB [19,20]. The second type of boundary condition is developed according to the Maxwell model [21]. Therein, correlations are employed involving first- and second-order velocity gradients at the wall to impose a slip velocity at the solid boundary. The Maxwell model is generally consistent with the gas kinetic theory, hence it has been extensively developed for different applications and different slip flow regimes [22–26]. Lastly, there have been attempts to include more grids, i.e., neighboring and next-neighboring nodes, using bounce-back and diffusive boundary conditions [23,27,28].

The estimation of the correct slip velocity when using a reduced number of grids requires further investigations. The effect of grid resolution was previously addressed in detail by Chai *et al.* [29], where they combined the bounce-back and the diffusive boundary condition to get a more accurate velocity slip. While models based on slip velocity magnitude are local and simpler in implementation, they typically lose generality in complex geometries such as three-dimensional (3D) porous media. There, it is challenging to determine the distance of every node to the nearest solid surface due to surface irregularities. Moreover, the numerical implementation becomes complicated in reacting flows, where all nondimensional numbers (Reynolds, Knudsen, and Damköhler numbers) are controlling the phenomena. The models based on the velocity derivatives are computationally more expensive due to the nonlocal information needed for the calculation of gradients at the solid walls. Nonetheless, these models impose the slip velocity at the wall and hence there is no need to alter any physical property. Using higher-order lattice Boltzmann methods by employing more neighboring grids has shown accurate results up to $\mathrm{Kn} = 0.2$, however the accuracy deteriorates as Kn approaches 1.0 [23].

In contrast to the velocity and temperature slip models (the latter being only relevant to thermal flows), there are very few studies on concentration slip and its influence on chemically reacting systems and specifically on the local catalytic reaction rate [2]. The main reason is that the concentration slip has a negligible impact for nonreactive (noncatalytic in the present work) simulations. However, it can appear in catalytic reactive flows with high surface Damköhler numbers. The earliest research dates back to Scott [30]. Afterwards, other researchers [31–33] focused on the concentration slip (or jump, as it is equivalently referred to), however the proposed models were obtained using similarity arguments and not a rigorous theory [34]. Moreover, the effect of chemical reaction at the surface was not considered [2].

Xu and Ju [34] derived velocity, concentration, and temperature jumps based on kinetic theory. Their model reduces to the older slip models [33,35] under specific conditions. In a later work, Zade *et al.* proposed a more general model for velocity, concentration, and temperature jumps based on gas kinetic theory [2]. They applied the model to investigate the effect of Damköhler number, Knudsen number, mass accommodation coefficient, and surface coverage in the catalytic reaction of hydrogen [36]. This model [36] has no simplifying assumptions and may thus appear superior to past slip models. Nevertheless, it is more complex due to several parameters involved in the adopted equations. Although there is a general consensus regarding the negligible effect of velocity slip on the catalytic reaction rate [34–36], a concrete conclusion regarding the impact of concentration slips has not yet been reached. The difficulty arises from the dependency of concentration jumps on other parameters such as the temperature jump. Whereas temperature jump can enhance the catalytic reaction rate [34], the impact of concentration jump on the reaction rate is still debatable. Xu and Ju [34] concluded that the concentration jump can increase the reaction rate, especially near the inlet of channels and particularly for radicals, but Zade *et al.* [36] reported that the concentration jump reduces the conversion of fuel. In addition, Zade *et al.* [36] showed through numerical simulation that the mass accommodation coefficient has little to no effect on the catalytic reaction rate. These results appear to contradict those obtained by Xu and Ju [34].

The nonpassive scalar approaches for the simulation of gas mixture flows can be categorized into three groups: models based on equilibrium function modification [37–40], models based on forcing terms [41–43], and multispeed models [44,45]. Recently, new models have been proposed for binary mixtures [46] and multicomponent gas mixtures [47], with the latter further extended to thermal and gas-phase reactive flows [48,49].

The catalytic boundary condition is mostly treated as a source/sink term in passive-scalar approaches, whereby it alters the concentration of species and does not noticeably change the mixture transport and thermodynamic properties. This assumption is strictly valid when the reaction is equimolar (no volume change and hence no reaction-induced flow acceleration or deceleration) and the species have very similar transport properties or when the solution is dilute in reactants

such that the effect of species conversion on the mixture can be neglected. However, the passive scalar assumption can be violated for nonequimolar reactions, where there can be a large volume change between reactants and products. Under such conditions, not only is a nonpassive scalar approach required, but also the LB catalytic boundary condition should be consistent in terms of mass, momentum, and pressure. To the authors' best understanding, there is no study with a nonpassive scalar multicomponent gas mixture model in the presence of strongly nonequimolar reactions using the lattice Boltzmann method. Previous research has mostly focused on equimolar reactions [50–53]. Van den Akker *et al.* [40] performed numerical simulations in a catalytic channel with a nonequimolar reaction (a volume increase of 50%) with the goal to show that their multicomponent model is capable of dealing with different speeds of sound; nonetheless, the accuracy of the catalytic boundary condition was not addressed.

In the present work, a catalytic LB boundary condition is proposed that is applicable for both equimolar and nonequimolar isothermal reactions and which explicitly includes the diffusion coefficients of all species. The accuracy of the adopted diffusive boundary condition is evaluated for reactive and nonreactive simulations in the continuum and slip flow regimes, for a large and a reduced number of grids. The proposed catalytic boundary condition is finally extended to incorporate concentration jumps in the slip flow regime, while the impact of combined velocity slips and concentration jumps is investigated in detail.

II. MULTICOMPONENT LATTICE BOLTZMANN MODEL

The two-dimensional (2D) multicomponent lattice Boltzmann model originally proposed by Arcidiacono *et al.* [44] was extended for 3D simulations and arbitrary Damköhler numbers in our previous study [53]. Herein, a short review of the model in [44] is presented to facilitate the discussion and derivation of the new LB model.

The discrete-velocity kinetic equation for each species is as follows:

$$\partial_t f_{ji} + c_{ji\alpha}\partial_\alpha f_{ji} = -\frac{1}{\tau_{j1}}(f_{ji} - f^*_{ji}) - \frac{1}{\tau_{j2}}\left(f^*_{ji} - f^{\mathrm{eq}}_{ji}\right) + \Psi_{ji},$$
$$j = 1, 2, \ldots, N, \quad i = 0, 1, \ldots, 26, \tag{1}$$

where f_{ij} is the distribution function for species j, and i refers to the discrete lattice direction. A 3D lattice structure with 27 discrete velocities (D3Q27) is considered, hence i varies from 0 to 26. Each species' discrete velocity $c_{ji\alpha}$ ($\alpha = x$, y, and z) is a function of the species' molar mass (M_j) and the discrete velocity vector ($e_{i\alpha}$) as $c_{ji\alpha} = c_j e_{i\alpha}$. c_j is scaled based on the lightest species' molar mass (M_L) as $\sqrt{M_L/M_j}$. The values of $c_{ji\alpha}$ for a D3Q27 lattice are provided in Ref. [53]. f^*_{ji} and f^{eq}_{ji} are the quasiequilibrium and equilibrium functions, respectively [53]. The discretized kinetic equation is provided in the Appendix

The present multicomponent model uses the multispeed approach to handle the species' different speeds of sound. For this purpose, the main lattice domain is structured based on the lightest species, with the highest speed of sound being equal to 1 in the LB unit. While the particles of the lightest species can move one lattice spacing in one LB time step, leading to a unity speed of sound, the other species' particles move a shorter distance. Hence, an extrapolation is required to transfer information to the nodes defined in the main lattice domain. The streaming step includes the extrapolations for all species other than the lightest one.

Equation (1) must be solved for all N species. The term Ψ_{ji} in the right side of the equation is needed to satisfy momentum conservation up to second order, and it will be discussed later on. The equilibrium distribution function f^{eq}_{ji} is obtained by minimizing the entropy function with two constraints [5,54], and it is written as

$$f^{\mathrm{eq}}_{ji}(\rho_j, u) = \rho_j \prod_{\alpha=x,y,z} \frac{2c^2_{Li\alpha} - 1}{2^{c^2_{Li\alpha}}}\Big(\big(c^2_{Li\alpha} - 1\big) + \sqrt{M_j}c^2_{Li\alpha}u_\alpha + M_j u^2_\alpha + T\Big), \tag{2}$$

where T is the temperature, ρ_j is the individual species densities, and $c_{Li\alpha}$ is the species discrete velocity for the lightest species. The species densities ρ_j, momenta $J_{j\alpha}$, and concentrations C_j are computed as

$$\rho_j = \sum_{i=0}^{i=26} f_{ji}, \quad J_{j\alpha} = \sum_{i=0}^{i=26} f_{ji}c_{ji\alpha}, \quad C_j = \frac{\rho_j}{M_j}. \tag{3}$$

Similarly, the total mixture density, momenta, and concentration are obtained as

$$\rho = \sum_{j=1}^{j=N} \rho_j, \quad J_\alpha = \sum_{j=1}^{j=N} J_{j\alpha}, \quad C = \sum_{j=1}^{j=N} C_j. \tag{4}$$

The mixture velocity U_α is then equal to J_α/ρ.

The quasiequilibrium distribution function is then derived by replacing the mixture velocity with the species velocities in Eq. (2) [5,54]:

$$f^*_{ji}(\rho_j, u_j) = \rho_j \prod_{\alpha=x,y,z} \frac{2c^2_{Li\alpha} - 1}{2^{c^2_{Li\alpha}}}\Big(\big(c^2_{Li\alpha} - 1\big) + \sqrt{M_j}c^2_{Li\alpha}u_{j\alpha} + M_j u^2_{j\alpha} + T\Big), \tag{5}$$

where $u_{j\alpha}$ is calculated as $u_{j\alpha} = J_{j\alpha}/\rho$.

The multicomponent gas mixture model incorporates the species diffusivity and dynamic viscosity through two separate relaxation times (τ_{j1} and τ_{j2}). For the sake of brevity, the derivations are not discussed here and only the final relations are presented. The dynamic viscosity of the mixture (μ) is related to the species concentration, first relaxation time (τ_{j1}), and temperature as follows [51]:

$$\mu = \sum_{j=1}^{N} (\tau_{j1} C_j T). \tag{6}$$

The individual species dynamic viscosities (μ_j) are linked to the mixture viscosity (μ) via the empirical Wilke formula [55]:

$$\mu = \sum_{j=1}^{N} \frac{X_j \mu_j}{\sum_k^N X_k \varphi_{jk}}, \tag{7}$$

where X_j is the mole fraction of species j, and φ_{jk} is calculated as

$$\varphi_{jk} = \frac{1}{\sqrt{8}}\left(1+\frac{M_j}{M_k}\right)^{-1/2}\left[1+\left(\frac{\mu_j}{\mu_k}\right)^{1/2}\left(\frac{M_k}{M_j}\right)^{1/4}\right]^2. \quad (8)$$

Finally, the relaxation times τ_{j1} are obtained by comparing Eqs. (6) and (7) as

$$\tau_{j1} = \frac{\mu_j}{p\sum_k^N X_k \varphi_{jk}}. \quad (9)$$

On the other hand, the relaxation times τ_{j2} are related to the mixture-average species diffusivities D_{jm} [44]:

$$\tau_{j2} = \frac{\rho_j}{P_j} D_{jm}, \quad (10)$$

where P_j is the partial pressure of species j, and D_{jm} is calculated as [56]

$$D_{jm} = \frac{1-Y_j}{\sum_{k\neq j}^N X_k/D_{jk}}, \quad (11)$$

where Y_j is the mass fraction of species j, and D_{jk} is the binary diffusion coefficient between species j and k.

The more advanced multicomponent models based on the Maxwell-Stefan diffusion model [49,57] could be used to describe other complicated phenomena such as countergradient diffusion or osmotic diffusion. However, such phenomena are not relevant in the current isothermal catalytic channel-flow simulations. Only in the presence of strong temperature gradients can countergradient diffusion be observed in channels with catalytic reactions as we reported in [58].

The total correction term Ψ_{ji} is introduced in Eq. (1) to conserve momentum and the pressure tensor and is partitioned as

$$\Psi_{ji} = \Psi_{ji}^{\mathrm{I}} + \Psi_{ji}^{\mathrm{II}}, \quad (12)$$

The first correction term (Ψ_{ji}^{I}) is needed since the mixture-averaged diffusion approximation does not lead to momentum conservation [59]. Furthermore, the pressure tensor deviates from the macroscopic momentum equation [44]. To compensate for this deviation, the second correction is added (Ψ_{ji}^{II}). A detailed explanation of these correction terms can be found in [44,51].

III. CATALYTIC REACTIVE BOUNDARY CONDITION

When the numbers of moles of reactants and products are equal, the reaction is equimolar and conserves the volume after reaction. The most general reaction type is, however, the nonequimolar reaction, where the moles of the products can be either larger or smaller than the moles of the reactants. Of particular interest in the present study is to develop an LB model applicable for strongly nonequimolar reactions, as the associated large volume change will be shown to directly impact the catalytic boundary condition. For example, chemical synthesis reactions proceed with mole and hence volume reduction (e.g., ammonia synthesis with 50% reduction: $N_2 + 3H_2 \rightarrow 2NH_3$), while reforming reactions typically increase the volume (e.g., methane reforming with 100% increase: $2CH_4 + O_2 \rightarrow 2CO + 4H_2$). Such strongly nonequimolar reactions appreciably change the mixture volume and density. Moreover, the mixture's speed of sound is a function of the mixture's average molar mass $\overline{M}$ as $c_s = \sqrt{\frac{\gamma RT}{\overline{M}}}$ [51]. The difference in mixture average molar mass between reactants and products leads to a variation in the mixture's speed of sound in nonequimolar reactions.

Simulation of systems with heterogeneous (catalytic) chemical reactions should meet two requirements: a consistent nonpassive scalar multicomponent model, and a proper catalytic boundary condition. At the gas-solid interface, while a passive scalar LB approach can accurately predict equimolar and isothermal reactions as there is no volume change (either due to nonequimolar reaction or due to reaction exothermicity/endothermicity) and hence no change in velocity and mixture density, it fails in simulating nonequimolar reactions (isothermal or nonisothermal) since the reaction is allowed to only alter the species concentration but not all macroscopic properties of the mixture. The simulation of both equimolar and nonequimolar reactions is widely studied using conventional Navier-Stokes CFD solvers. However, the effect of nonequimolar catalytic reactions has not been elaborated in LB models.

Contrary to the conventional CFD catalytic boundary condition or even the equilibrium LB boundary condition, where macroscopic properties such as density are directly imposed, the diffusive LB boundary condition changes only the missing populations. This feature renders the diffusive boundary condition second-order accurate, while the equilibrium boundary conditions are generally first-order accurate [4].

A. Catalytic reactive boundary condition for equimolar reactions

In our previous study, we introduced a catalytic boundary condition based on the diffusive model for an arbitrary surface (i.e., catalytic) Damköhler number (Da_s), which is defined as

$$\mathrm{Da}_s = \frac{kl}{D_{jm}}, \quad (13)$$

where k is the reaction rate coefficient, l is a characteristic length, which for the channel-flow geometry studied herein is the channel height ($l = h$), and D_{jm} is the mixture-average diffusivity [see Eqs. (10) and (11)] of the species controlling the reaction. Considering an irreversible first-order reaction with two reactants and two products ($b_1A + b_2B \rightarrow b_3C + b_4D$), where one of the two reactants is deficient and the other is in excess, the reaction-diffusion mass balance at the catalytic wall can be written as

$$S_j \equiv b_j M_j k C_{dw} = \rho_w D_{jm}\left(\frac{\partial Y_j}{\partial y}\right)_w, \quad (14)$$

where S_j is the catalytic reaction rate of any species j, depending only on the deficient (subscript d) reactant concentration at the wall (C_{dw}), b_j is the species stoichiometric coefficient, and the subscript w indicates values at the reactive wall. Due to the dependency of the reaction rate on the local value of the deficient reactant's concentration, Eq. (14) can be solved for C_{dw}. The final equation to calculate the incoming populations f_{ij}^{in} (see Fig. 1) based on the diffusive LB boundary condition

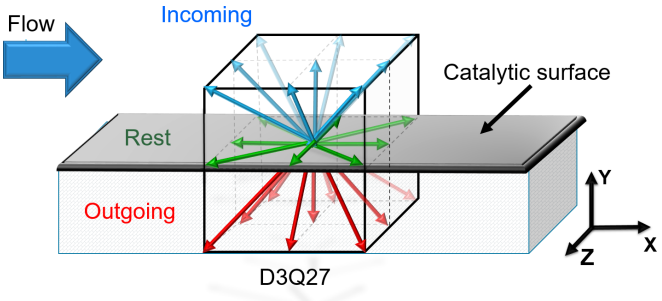

FIG. 1. Definition of incoming, rest, and outgoing populations for a D3Q27 lattice at the surface of a catalyst.

for a D3Q27 lattice can be written as [53]

$$f_{ji}^{\text{in}} = f_{ji}^{\text{eq}}(\rho_w, U_w)\frac{\sum_{i=0, f_{ji}c_{ji\alpha}n_\alpha<0}^{i=26} |f_{ji}c_{ji\alpha}n_\alpha| + \frac{b_j M_j C_{dn}}{\frac{b_d \delta y}{D_{dm}} + \frac{1}{k}}}{\sum_{i=0, f_{ji}c_{ji\alpha}n_\alpha>0}^{i=26} \left|f_{ji}^{\text{eq}}(\rho_w, U_w)c_{ji\alpha}n_\alpha\right|}, \tag{15}$$

where C_{dn} is the concentration of deficient species in the near-wall (subscript n) gas node located along the wall-normal direction (the Y direction in Fig. 1) at a distance δy from the wall. In the right-side quotient of Eq. (15), the first term in the numerator is the mass flux of species j leaving the given reactive node (related to the outgoing populations in Fig. 1) and the second term corresponds to the reaction rate S_j, which is positive for products and negative for reactants. The denominator is the incoming mass flux towards the catalytic surface (related to the incoming populations in Fig. 1), calculated from the equilibrium populations f_{ji}^{eq}. This catalytic boundary condition is reduced to the reaction rate used in past studies [50–52] in the limit of very low reaction rates (low surface Damköhler numbers, $\text{Da}_s \ll 1$). Moreover, Eq. (15) can correctly predict the wall concentration and reaction rate in the mass-transport-controlled regime ($\text{Da}_s \gg 1$) [53]. While Eq. (15) was employed and validated for equimolar reactions such as the total oxidation of methane ($CH_4 + 2O_2 \rightarrow CO_4 + 2H_2O$) and for a wide range of surface Damköhler numbers [53], it does not explicitly include the diffusion coefficient of each species in the calculation of its reaction rate. However, the reaction-diffusion interfacial (gas-solid) balance of a species other than the deficient reactant is a function not only of the stoichiometric coefficient, molar mass, reaction rate coefficient, and the concentration of the deficient species, but also of the diffusivity of the species in question. This old treatment in Eq. (15) implies that each species cannot diffuse away or towards the catalytic surface correctly, because the reaction-diffusion Eq. (14) is not properly satisfied for all species. This may not be an overriding issue for equimolar reactions, as they typically involve species having not very different diffusivities.

Solving the reaction-diffusion Eq. (14) will not necessarily guarantee mass conservation at the reactive wall, when the species diffusion coefficients are very different from D_{dm}. To investigate the resulting error, one needs to sum up the right and left sides of the equation. Although the left side (reaction terms) sums up identically to zero, the total diffusive flux is nonzero:

$$R = \sum_j^N \left[\rho_w D_{jm}\left(\frac{\partial Y_j}{\partial y}\right)_w\right] \neq 0, \tag{16}$$

where R is the total diffusive mass flux error. One common remedy for Eq. (16) is the introduction of a correction term to compensate for the error due to different diffusion coefficients. However, this requires an iterative approach as detailed in Ref. [60].

B. Catalytic reactive boundary condition for equimolar and nonequimolar reactions

A modified catalytic reactive boundary condition is proposed, which is consistent with the reaction-diffusion equation for all species. For this purpose, a correction term similar to the velocity correction widely used in conventional CFD methods [60] is introduced. It will be shown that this correction term leads to a fixed total pressure boundary condition at the reactive wall as well.

A mass source term in the kinetic Eq. (1) typically modifies the zeroth-, first-, and second-order moments at a given node. Therefore, special consideration is required, especially for multicomponent gas mixtures. Although species properties such as velocity and partial pressure change during a reaction, the total mixture velocity and pressure should remain constant. A constructed catalytic boundary condition based on mass flux density (ρU) is accurate, provided that the mixture density does not change due to catalytic reaction. This is valid for equimolar reactions such as the total oxidation of methane. However, this mass flux definition leads to a mixture velocity change for nonequimolar reactions. The change in total mixture density requires that the total mixture velocity at the boundary should vary accordingly, such that the mass flux of the mixture before and after reaction remains constant. The conservation of mass flux is a basic requirement in catalytic systems where neither accumulation of species on the catalyst (deposition) nor consumption of the solid catalyst (etching) occurs.

Herein, we construct a boundary condition based on the mixture pressure. Since the total mixture pressure is constant at the gas-solid interface, the influence of the mass source/sink term in Eq. (1) should be evaluated. An effective reaction rate for species j ($S_{j,\text{eff}}$) is defined as follows:

$$S_{j,\text{eff}} = S_{j,0} - F_{\text{corr},j}/c_{js}, \quad S_{j,0} = \frac{b_j M_j C_{dn}}{\frac{b_d \delta y}{D_{dm}} + \frac{1}{k}}, \tag{17}$$

where c_{js} is the speed of sound of species j, and $F_{\text{corr},j}$ is the correction term applied for each species with $F_{\text{corr},j} = F_{\text{corr}} Y_j$ such that $\sum_j^N (F_{\text{corr},j}) = F_{\text{corr}}$. The mass fractions Y_j partition the total correction term among different species. F_{corr} is calculated such that the effect of the mass source/sink term on total pressure vanishes. Since the source/sink term unit is gr/(cm^2 s), by multiplying this term with the species' speed of sound c_{js}, summing up over all species, and using Eq. (14), the total correction term becomes

$$F_{\text{corr}} = \sum_j^N (S_{j,0} c_{js}) = \sum_j^N (b_j M_j k C_{dw} c_{js}). \tag{18}$$

The magnitude of the correction term depends on the reaction rate and the species' speed of sound ($c_{js} = \frac{1}{\sqrt{M_j}}$). While the correction term is calculated based on a fixed mixture pressure, it is possible to show that it is analogous to the velocity correction used in CFD methods [59,61].

According to Graham's law, the ratio of the rate of mass diffusion of species j (F_{Dj}) to the mass diffusion rate of species k scales as

$$\frac{F_{Dj}}{F_{Dk}} = \frac{\sqrt{M_j}}{\sqrt{M_k}}. \tag{19}$$

The species transport and thermodynamic properties in the present multicomponent LB model can be defined based on the deficient species' properties (referred to by subscript d). Hence, Eq. (19) can be used in Eq. (16) as follows:

$$R = \sum_j^N (F_{Dj})_w = \sum_j^N \left(F_{Dd} \frac{\sqrt{M_j}}{\sqrt{M_d}} \right)_w. \tag{20}$$

Substituting Eq. (14) into Eq. (20),

$$R = \sum_j^N (b_d k C_{dw} \sqrt{M_d M_j}). \tag{21}$$

Equation (21) can be simplified further since $c_{js} = \frac{1}{\sqrt{M_j}}$. Consequently, the error term calculated from the mass diffusion flux is

$$R = \sum_j^N (b_d \sqrt{M_d} M_j k C_{dw} c_{js}). \tag{22}$$

The obtained relation is very similar to the correction term in Eq. (18). The only difference appears in the stoichiometric coefficient. Moreover, the correction term defined in Eq. (18) is analogous to the velocity correction term in standard CFD models. Therefore, the applied correction not only ensures fixed mixture pressure but also incorporates diffusive flux differences among species due to different diffusion coefficients.

Contrary to some particular conditions such as dilute solutions, low reactivity (low Da_s), or a gas mixture containing species with very similar molar masses and diffusion coefficients, where the error term can be negligible, the error deteriorates the accuracy of the numerical simulation and must be considered in a general catalytic boundary condition. An inconsistent mass source/sink term can further lead to pressure fluctuation in the simulation domain that in turn affects the velocity field in the transient part of the solution.

Besides mass conservation, the correction term fixes the total mixture pressure at the wall and improves the stability of the numerical simulation. In addition to the mass flow rate, the species velocity used in the diffusive boundary condition [Eq. (15)] should be modified. As discussed before, the species' mass, velocity, and partial pressure are altered through the source/sink term. However, the species' velocity in the equilibrium function used in the diffusive boundary condition must be consistently set. In the original model [44], it is assumed that the species' velocities are equal to the total mixture velocity at the wall (U_w). However, this assumption can be violated, especially when one or more species diffuse much faster than others. This typically happens in strongly nonequimolar reactions, which are accompanied by large changes in species molar masses and hence in species diffusivities. For example, such differences are observed in the nonequimolar biomass methanation reaction ($3H_2 + CO \rightarrow CH_4 + H_2O$), where the molar mass ratio between the heaviest species (CO) and the lightest one (H_2) is 14. This leads to hydrogen diffusing much faster than the other heavier molecules.

Herein, it is suggested that the diffusive velocity ($V_{j\alpha}$) is employed in addition to the wall velocity (U_w) for every species in the catalytic boundary condition. The diffusive velocity can be calculated as

$$V_{j\alpha} = -(U_\alpha - U_{j\alpha}). \tag{23}$$

This velocity is also consistent with the peculiar-diffusive reflection model with the Maxwellian distribution function suggested by Grad [62]. It is worth noting that the summation of the species diffusive velocities is zero with the diffusive velocity correction of Eq. (12). This feature guarantees that the second assumption, i.e., fixed mixture velocity at the reactive wall, is not violated. Therefore, with the two new modifications, two conditions regarding constant total pressure and constant mixture velocity for a catalytic reactive model are satisfied.

The final form for a first-order reaction rate used in Eq. (17) is

$$S_{j,\mathrm{eff}} = S_{j,0} - (Y_j / c_{js}) \sum_j^N (S_{j,0} c_{js}). \tag{24}$$

Although the above discussion considered only first-order reactions, a similar approach can be applied to calculate the correction term for reaction rates with arbitrary orders and dependence on all reactants. For example, one can treat the concentration of other reactants as a known quantity obtained from the previous time step. This time-splitting treatment is acceptable given the small time steps in LB, leading to a similar equation to Eq. (14). For arbitrary reaction rate orders, an iterative procedure via a Newton solver is required to solve the reaction-diffusion equation [Eq. (14)] for the deficient species [53]; afterwards, the correction term mentioned above can be easily calculated for all other species. It is nonetheless stressed that first-order reaction rates are quite common in many applications, such as the oxidation of hydrocarbons on noble metals [63,64].

IV. VELOCITY AND CONCENTRATION SLIP MODELS WITH DIFFUSIVE BOUNDARY CONDITION

For small Knudsen numbers ($\mathrm{Kn} < 0.1$) with reduced grid points ($N < 10$) in the wall-normal direction, a correct slip model must minimize all existing errors. The error originates from the nonlocality of the slip velocity boundary condition [65] and from the discretization [4]. Furthermore, the slip velocity should have a general form, such that all simulations in geometries with varying Knudsen number are properly modeled at every location.

The diffusive boundary condition is the only boundary condition that intrinsically has the potential to estimate slip

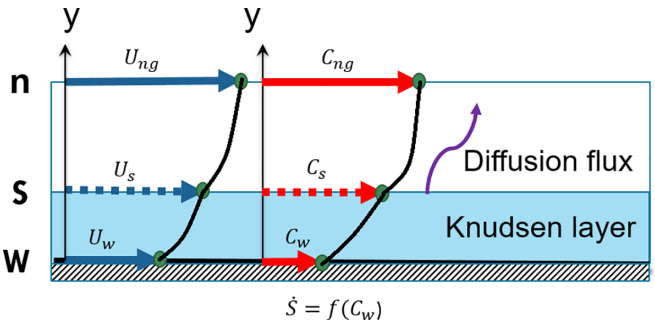

FIG. 2. Schematic of velocity and concentration slips in the presence of a Knudsen layer.

velocity when the Knudsen number is relatively high. The validity of the diffusive boundary condition for a wide range of Knudsen numbers (up to 2.0) has been studied in several past works, using the first and second velocity derivatives at the solid wall [14,22,24,25]. These studies have mostly focused on the development of models with the capacity to predict slip velocities for a particular range of Knudsen numbers with a well-resolved grid. However, one of the main applications of slip velocity models is the simulation of fluid flow in micro- and nanochannels such as microfluidics, rocks, fluidized bed porous particles, etc., where numerous interconnected channels/pores must be simulated simultaneously. For such cases, it is computationally prohibitive to refine all the microchannels with enough grid points.

Figure 2 shows a schematic of the Knudsen layer and the velocity and concentration slips. As depicted in Fig. 2, the catalytic reaction occurs at the wall while the diffusion flux equation is valid at the edge of the Knudsen layer and not in the Knudsen layer [36]. Therefore, the reaction-diffusion equation solved in the previous section should be modified accordingly to incorporate the effect of concentration and velocity jumps.

The slip velocity model proposed by Maxwell [21] is adopted in this paper. It is one of the fundamental descriptions based on gas-solid interaction [3]. The model was later improved for higher Knudsen numbers by several authors [17,66–68]. The isothermal form of the slip velocity model for small Knudsen numbers (Kn $\ll$ 1) is written as [21]

$$u_s = U_w + A_1 \mathrm{Kn}\left(\frac{\partial u_s}{\partial n}\right)_s, \tag{25}$$

where n is the normal to the surface direction, and u_s is the slip velocity. Kn is the Knudsen number of the flow depending on the fluid physical properties and channel size. $A_1 = \frac{2-\alpha_t}{\alpha_t}$ is the slip coefficient, which is a function of the tangential momentum accommodation coefficient α_t and the Knudsen number [65]. Here, A_1 is considered constant and no longer affects the ensuing discussion. Equation (25) is generally accurate for Kn < 0.05 [3]. However, it cannot predict the Knudsen paradox, and the accuracy of the Maxwell model reduces as Knudsen increases [65]. To compensate for this deficiency, an appropriate slip boundary condition requires not only the first but also the second velocity derivative [67].

The slip velocity is considered through the equilibrium function in the diffusive boundary condition. The implementation for curved boundaries as well as moving boundaries is straightforward, as discussed in Refs. [15,69]. Equation (25) can be used for multicomponent gas mixtures by considering the corresponding Knudsen numbers for each species:

$$\mathrm{Kn}_j = \frac{\lambda_j}{L_0} = \sqrt{\frac{\pi\gamma}{2}}\frac{\mathrm{Ma}_j}{\mathrm{Re}_j}, \tag{26}$$

where j is the species index, Ma_j is the Mach number, Re_j is the Reynolds number, γ is the ratio of specific heats, and λ is the mean free path. By substituting $\mathrm{Ma}_j = \frac{U_j}{c_{sj}}$ and $\mathrm{Re}_j = \frac{UL_0}{\nu_j}$ into Eq. (26) and considering the definition of the speed of sound, the following relation for the Knudsen number in LB can be derived for each species in the mixture:

$$\mathrm{Kn}_j = \sqrt{\frac{\pi\gamma}{2}}\frac{\tau_j T c_{sj}}{H}, \tag{27}$$

where all parameters should be in units of LB. H is the number of grid points across the channel, T is the reference temperature in units of LB ($T = \frac{1}{3}$), and γ is equal to 2 and $\frac{5}{3}$ for two- and three-dimensional flows, respectively [51]. The obtained relation in Eq. (27) is of interest for practical reactive flows where the spatial and temporal properties of the mixture vary.

The Knudsen number from Eq. (27) is consistent with kinetic gas theory in the investigated Knudsen number range (up to 0.2). The slip velocity for a gas mixture flow is calculated and imposed for every species separately, hence the effect of slip velocity for every species varies depending on the physical parameters of each species at a given location.

Using Eq. (25) with a reduced number of grid points, however, results in overestimation of the slip velocity due to the appearance of numerical slip velocity. The slip velocity predicted by Eq. (25) is higher than the theoretical one for an arbitrary relaxation time. The error appears, similarly to the bounce-back boundary condition, from the dependency of the actual wall location on the relaxation time. While the model gives sufficiently accurate results for very low relaxation times, the error increases as the relaxation time increases. In this work, we evaluate the error by applying the velocity slip model. The slip velocity can be calculated from Eqs. (25) and (26) as

$$u_{js} = U_w + A_1\sqrt{\frac{\pi\gamma}{2}}\frac{\tau_j T c_{sj}}{H}\left(\frac{\partial u_{js}}{\partial n}\right)_s. \tag{28}$$

The second term in Eq. (28) sets the slip velocity based on the velocity gradient. The implementation of the slip velocity model is independent of the reactivity of the solid wall (catalytic or noncatalytic). Equation (28) sets the first-order slip velocity at different Knudsen numbers. However, the numerical slip adds up as the Knudsen number increases. To eliminate the effect of the numerical slip velocity due to discretization, the velocity at the actual catalytic boundary, which is located midway between the computational boundary node and the neighbor node [4], should be first forced to be zero. For the fullway boundary approach used in this study, the velocity of the neighbor node with a negative sign ($-U_n$) is then added to the right-hand side of Eq. (28). This approach leaves only a small numerical error at low-to-moderate

Knudsen numbers (Kn < 0.1), even when a limited grid of 10 points is used across the channel.

Xu and Ju [34] defined slip models for velocity, concentration, and temperature based on the approximate solution of the Boltzmann equation. A similar equation to the slip velocity is considered for the concentration slip in an isothermal flow:

$$C_{js} = C_{jw} + A_2 \lambda_j \left(\frac{\partial C_{js}}{\partial n} \right)_s, \tag{29}$$

where A_2 is defined as $\frac{2-\alpha_{m,j}}{\alpha_{m,j}}$, and $\alpha_{m,j}$ is the mass accommodation coefficient, which is the same for all species [34]. In Eq. (29), it is assumed that the velocity gradient has a negligible impact on the concentration jump [33] (as shown by Zade *et al.* [36]). The obtained equation has an implicit form. The concentration slip model of Eq. (29) is adapted and incorporated into the present catalytic boundary condition.

In addition to the effect of velocity jump on the velocity field and of the temperature jump on the temperature field, both jumps theoretically affect the concentration slip as well [34]. Therefore, a concentration jump model must include both velocity and temperature jumps (the latter for thermal flows). It has been shown that the effect of velocity slip on the concentration jump is negligible [34,36], hence it is not further discussed in this paper. However, the effect of temperature jump on the concentration slip needs further investigation. Our model is derived in the presence of a temperature jump effect on the concentration slip, even though the current simulations are isothermal. The obtained equation gives a better insight into the impact of concentration jump and the possible effect of temperature jump on the reaction rate through the concentration jump. The following form of the density jump model is considered [35]:

$$\rho_{jw} = \sqrt{\frac{T_s}{T_w}} \left[\rho_{j,s} - \frac{2-\alpha_{m,j}}{\alpha_{m,j}} \lambda_j \left(\frac{\partial \rho_{j,s}}{\partial n} \right)_s \right], \tag{30}$$

where the subscripts w and s refer to the values at the reactive wall and the edge of the Knudsen layer (slip), respectively. Equation (30) shows that the temperature jump (T_s) has an important effect not only directly through the temperature slip model and reaction rate constant, but also via the concentration jump. While the temperature jump increases the reaction rate by increasing the reaction rate coefficient and species diffusivities, its presence in the concentration jump has an adverse effect [36]. It has been concluded that the concentration jump becomes important in isothermal flows only if the surface Damköhler number is large [34].

Equation (30) provides crucial information regarding the influence of temperature, Damköhler number, Knudsen number, and mass accommodation coefficient. However, this equation is implicit such that these influences cannot be easily exposed. For example, the effect of temperature jump on reaction rate in comparison to other parameters such as Da_s, Kn_j, and $\alpha_{m,j}$ is not distinguishable. Furthermore, the incorporation of concentration jump into the present catalytic diffusive boundary condition has not been attempted in past literature.

To obtain an explicit equation for the reaction rate as a function of the aforementioned parameters, a similar approach to Khatoonabadi *et al.* [53] is followed. The difference with the no-slip boundary condition is that the diffusion flux $[\rho D_{dm} (\frac{\partial Y_d}{\partial y})_s]$ is valid at the edge of the Knudsen layer and not at the reactive wall, while the reaction rate is a function of wall concentration/density. Using Eqs. (14) at the edge of the diffusive layer and Eq. (30), the density of the deficient species ρ_{dw} can be obtained as

$$\rho_{dw} = \frac{\rho_{dn}}{\sqrt{\frac{T_w}{T_s}} + \frac{b_d k \delta y}{D_{dm}} - A_2 \mathrm{Da}_{ds} \mathrm{Kn}_d}. \tag{31}$$

Finally, the catalytic reaction rate can be derived from Eq. (14) as

$$S_j = \frac{b_j M_j k C_{dn}}{\sqrt{\frac{T_w}{T_s}} + \frac{b_d k \delta y}{D_{dm}} - A_2 \mathrm{Da}_{ds} \mathrm{Kn}_d}. \tag{32}$$

Equation (32) can be utilized in the diffusive boundary condition [Eqs. (15) and (24)] instead of $S_{j,0}$. The main advantage of Eq. (32) over the previous implicit form [Eq. (30)] is that the impact of the controlling parameters can be theoretically evaluated to determine under which conditions the effect of concentration jump on the reaction rate is negligible.

First, the temperature can modify the reaction rate depending on the ratio of wall-to-gas temperature. This influence is on top of the temperature jump and the dependence of the reaction rate constant (k) on temperature. When the wall temperature is higher than the inlet temperature in a channel configuration, the temperature jump has an adverse effect on the reaction rate. This result is consistent with simulation results from Ref. [36]. Second, Eq. (32) exemplifies the impact of the Knudsen number under particular conditions. There are two conditions under which the concentration jump plays a significant role in the reaction rate; the impact can be large due to either a high surface Damköhler number ($\mathrm{Da}_s \gg 1.0$) or a very low mass accommodation coefficient ($\alpha_{m,j} \ll 1.0$). Third, Eq. (32) can be reduced to Eq. (15) for isothermal flows and low Knudsen numbers. It is noted that isothermal or nearly isothermal flows are relevant in many catalytic systems, such as exhaust gas pollutant abatement in automotive vehicles and electrocatalytic reactions in low-temperature polymer electrolyte fuel cells (PEFCs).

V. NUMERICAL RESULTS

In this section, the catalytic boundary condition [Eq. (15)] and the updated reaction rate in Eq. (24) together with the velocity and concentration slips [Eqs. (28) and (32)] are evaluated for a nonequimolar reaction in the continuum and slip flow regimes. In the first part, the biogas methanation reaction is simulated at a very small Knudsen number, and the results are validated against simulations with a finite-volume CFD code. Then, a single-component channel flow with nonreactive walls is studied numerically for a range of Knudsen numbers, and the velocity slip results are compared to DSMC data from the literature. Finally, a catalytic channel is considered at a higher Knudsen number to investigate the significance of velocity slips and concentration jumps. Steady-state results are presented for all simulations.

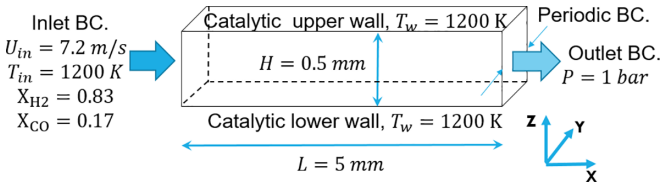

FIG. 3. Schematic of a three-dimensional catalytic channel with all boundary conditions.

A. Nonequimolar catalytic reaction

The model proposed in Sec. III is implemented to simulate the biogas methanation reaction ($3H_2 + CO \rightarrow CH_4 + H_2O$) in a catalytic channel. The molar ratio of the heaviest species (CO) to the lightest (H_2) species is 14, about five times higher than the corresponding ratio in the equimolar total oxidation of methane ($CH_4 + 2O_2 \rightarrow CO_4 + 2H_2O$) which was used in our past works [50,51,53].

The inlet mixture consists volumetrically of 83% hydrogen and 17% CO. CO is the deficient reactant, as the H_2:CO ratio is larger than the stoichiometric 3:1 ratio. Molar ratios of H_2 to CO between 3 and 6 are common in practical systems to avoid coking (carbon deposition) [70]. Needless to say, there is no limitation of any kind for the H_2:CO molar ratio in the present model. The pressure is atmospheric, while the inlet temperature is the same as the wall temperature ($T = 1200$ K) and they both remain constant during simulation. The channel length and height are 5 and 0.5 mm, respectively. The reaction rate follows the form of Eq. (14), being first order with respect to the deficient reactant CO. The reaction rate coefficient is $k = A\exp(\frac{-E_a}{RT_w})$, where $E_a = 77$ kJ/mol and $A = 3.81 \times 10^5$ cm/s. The surface Damköhler number based on the deficient CO reactant is 0.3, which is moderate and results in a mixed kinetics-transport controlled regime. The Knudsen number is very small ($\mathrm{Kn}_d \leqslant 0.001$) due to the large size of the channel height, therefore slip velocity is negligible in these simulations.

The Zu and He [71] boundary condition is applied at the channel inlet, and the species mole fractions as well as the inlet velocity ($U_{\mathrm{in}} = 7.2$ m/s) are imposed. Total mixture pressure at the outlet is specified at $P = 1$ bar through the equilibrium boundary condition. The inlet pressure and outlet velocity are unknown parameters. The inlet pressure is automatically adjusted during simulation such that the imposed inlet velocity is achieved. Since the original simulation tool is a D3Q27 hybrid code with the general-purpose computing on graphics processing units (GPGPU) but the CFD results used for validation are 2D, a periodic boundary condition is applied in the spanwise Y direction, and only three grid points are used in this direction (see Fig. 3).

Numerical simulations are carried out for two grid resolutions, 50×500 and 10×100 (in X and Z). We focus on the results obtained with the coarser grid due to the significance of low resolution in the simulation of complex geometries such as reactive porous networks. While the fine grid requires 500 000 time steps to reach steady state, the coarse grid converges within 150 000 time steps.

Similar to our previous study on the total oxidation of methane [53], the transport properties of all species at every node and every time step are calculated from the CHEMKIN transport package [59]. The simulation results are validated against a Navier-Stokes finite-volume CFD code. Details on the CFD code can be found in Refs. [53,72].

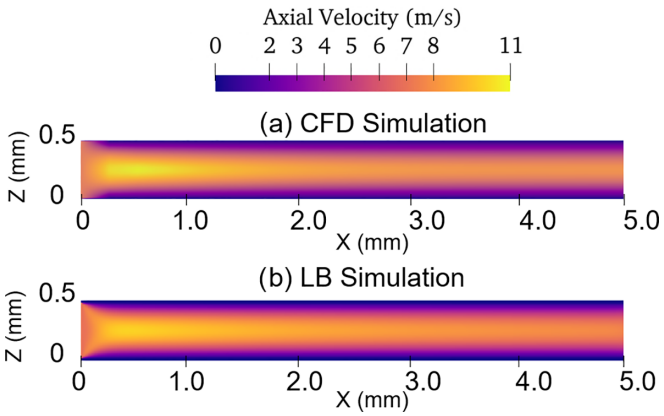

FIG. 4. Comparison of axial velocity contour obtained from CFD (top) and present lattice Boltzmann (bottom) methods with the same resolution (50×500); $\mathrm{Kn} = 0.001$, $\mathrm{Da}_s = 0.3$.

Figure 4 shows the mixture velocity contour in the channel using the newly developed reactive boundary condition of Eq. (24) in conjunction with Eq. (15) with 50×500 grid points for both LB and CFD. As shown in the contour plot, the mixture velocity in the bulk of the channel starts increasing at the beginning of the channel due to wall friction and no-slip condition at the wall; in other words, the flow develops from uniform at $X = 0$ towards a parabolic profile such that the midplane velocity initially increases. However, due to the volume-decreasing reaction, the mixture density increases with axial distance. Consequently, the velocity decreases, as more reactants are consumed at the catalytic wall, in order to keep the total mass flow rate $[\int_0^h \rho_{\mathrm{mix}}(z)u_{\mathrm{mix}}(z)\,dz]$ constant along the channel. The velocity peak location is generally a function of the entrance length (which itself is a function of the Reynolds number) and the strength of the reaction rate. In the absence of chemical reaction, the laminar flow in the plane channel would reach a fully developed velocity profile with the peak velocity 1.5 times higher than the uniform inlet velocity and would then remain constant. However, the chemical reaction at the channel walls increases the mixture density, leading to a drop of the maximum velocity along the channel. Finally, due to the nearly complete depletion of CO close to the outlet, the reaction rate becomes very low, and the mixture density and velocity remain almost constant. The velocity at the wall is zero in both simulations (no slip) at the studied very low Kn number. A small difference between the velocity profiles is observed only very close to the inlet when the flow is developing; otherwise, the profiles remain very similar in the rest of the channel.

The comparison between CFD and LB results at the midplane of the channel is presented in Fig. 5. The LB results are obtained for a coarse grid, where the channel height is discretized with 10 grid points. Generally, a very good agreement with the CFD simulation is achieved. The difference between the two simulation results at the outlet for mixture density and axial velocity is less than 2.9%. According to Fig. 5, the

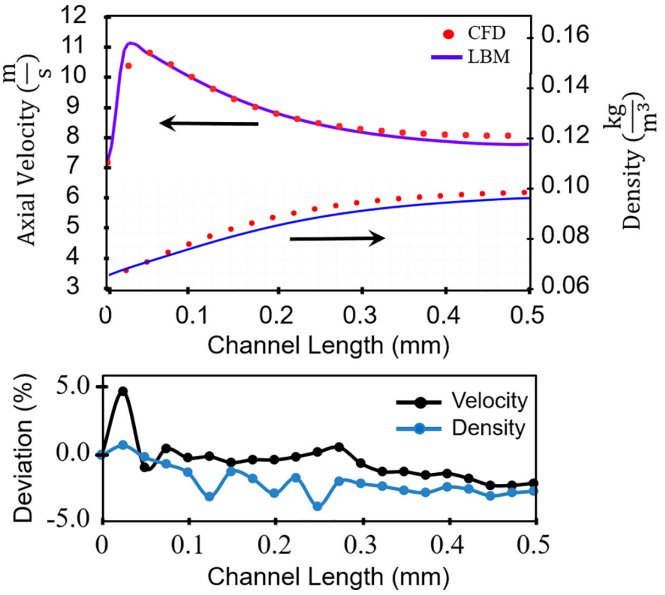

FIG. 5. Comparison of CFD and lattice Boltzmann simulation results along the midplane of the channel: top: axial velocity and mixture density, and bottom: deviation of LB from CFD results; grid resolution: 10×100 (LB) and 50×500 (CFD); Kn $= 0.001$, $\mathrm{Da}_s = 0.3$.

density increases around 50% along the channel. The variation of mixture density over the entire channel is illustrated in Fig. 6. The results show that the off-lattice multicomponent gas mixture model with a species molar mass ratio as high as 14 gives a quite accurate prediction. Using a finer LB grid (50×500) can improve the results modestly. The small difference between CFD and LB results may originate from the extrapolation due to different molar mass or different correction terms applied to calculate the reaction rate (as discussed previously).

Species mole fraction distributions are compared in Fig. 7. Since water and methane have similar molar masses and physical properties, the simulation results for these two species are similar and only the mole fraction of water is shown. A very

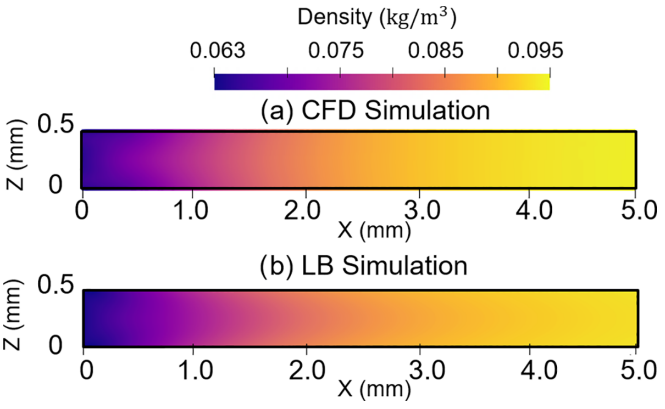

FIG. 6. Comparison of mixture total density along the channel obtained from CFD (top) and present lattice Boltzmann (bottom) methods with the same resolution (50×500); Kn $= 0.001$, $\mathrm{Da}_s = 0.3$.

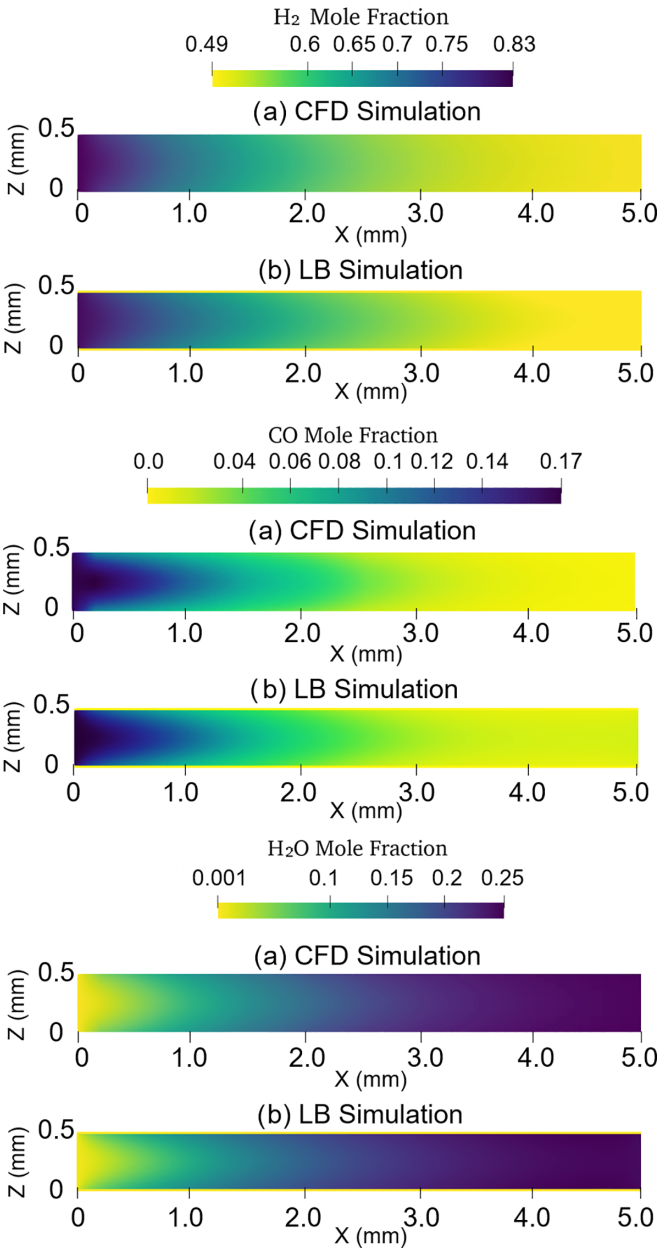

FIG. 7. Comparison of H_2, CO, and H_2O mole fraction distributions obtained with CFD and lattice Boltzmann simulations (50×500 grids); Kn $= 0.001$, $\mathrm{Da}_s = 0.3$.

good agreement between LB and CFD simulations is observed for all species. By comparing the distribution of hydrogen to that of other species, the hydrogen mole fraction is much more uniform across the channel (Z direction), a result of the much higher diffusivity of hydrogen. The hydrogen consumed at the reactive wall is quickly replenished by diffusive transport from the channel center, leading to small differences in its mole fraction across the channel at every axial X location.

Figure 8 shows the mole fraction of species at the channel midplane with reduced grids ($N_z = 10$). The LB simulation results match the CFD results very well. On the one hand, the correction term defined in Eq. (18) will be more significant

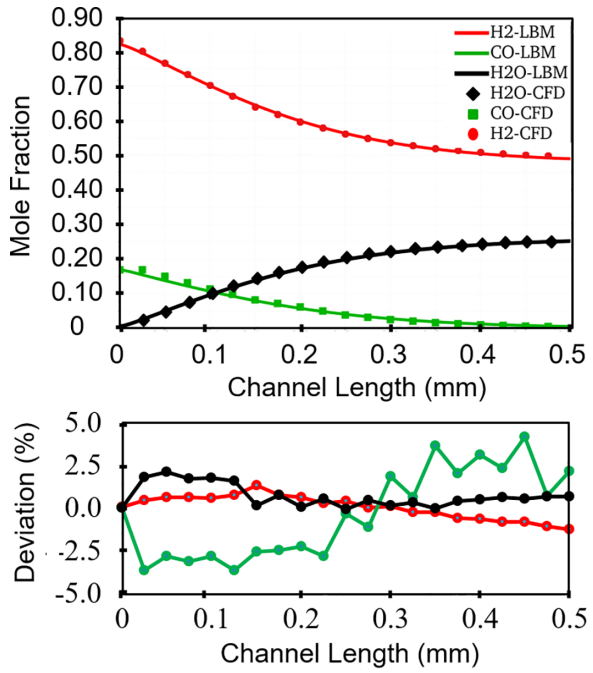

FIG. 8. Comparison of CFD and lattice Boltzmann simulation results along the channel midplane: top: H_2, CO, and H_2O mole fractions, and bottom: deviation of LB from CFD results; grid resolution: 10×100 (LB) and 50×500 (CFD); Kn $= 0.001$, $\mathrm{Da}_s = 0.3$.

at larger reaction rates and/or higher differences among the species' diffusion coefficients. On the other hand, it will be negligible for equimolar reactions and/or when the mixture species have very similar transport properties.

B. Slip velocity model

In this section, the slip model discussed in Sec. IV is implemented to simulate a gas flow in a microchannel. Although the model discussed before has a general form for every species in a gas mixture, a single component flow is considered here for the purpose of validation, since literature results are only reported for single-component flows.

In the simulations, the fluid in the channel consists of only hydrogen. The flow is isothermal, and the properties of hydrogen are calculated at a fixed temperature of 1200 K. To change the Knudsen number, the physical size (height) of the channel is varied such that three Knudsen numbers 0.04, 0.1, and 0.2 are investigated. For gas flows in a microchannel (channel height in the order of a few microns), the typical Knudsen number is smaller than 0.1. For example, hydrogen's mean free path is around 420 nm at 1200 K and 1 bar pressure. Therefore, a hydrogen gas flow in a channel with 4.2 μm height has a Knudsen number equal to 0.1.

Two grid resolutions are considered for every Knudsen number to study the effect of grid refinement. Figure 9 shows nondimensional velocity profiles across the channel height for different Kn numbers. The velocity is scaled with the average velocity. In addition to the slip velocity model [Eq. (28)], the velocity profile without the slip model (bare diffusive boundary condition model) is also shown in this figure. The simulation results are compared with DSMC by Kim *et al.* [23]. The velocity profile across the channel changes due to slip velocity. Since the mass flux along the channel is constant, the velocity at the center of channel decreases due to an increase in the slip velocity at the wall.

Even though the present collision model has two relaxation times corresponding to viscosity and diffusivity, neither of them is a free parameter. In addition, the ratio between these two parameters crucially determines the significance of diffusion and convection in the flow, therefore it is not prudent to modify the physics in order to reach a correct slip velocity. To evaluate further the error at different Knudsen numbers and resolutions, six different cases are considered. The slip velocity predicted by the diffusive boundary condition without the slip model is always larger than the DSMC values (Fig. 9). Despite the capability of the diffusive boundary condition in creating a slip velocity, the prediction of the bare model is not accurate, and the deviation between DSMC and LB results increases as the Knudsen number increases. The grid refinement can improve the results at higher Kn (Kn > 0.1) without any slip model, but the error is still relatively large. For instance, the error in slip velocity predicted by the bare model at Kn $= 0.1$ with discretization of 10 grid points is approximately 80% while a finer grid ($N = 50$) reduces the numerical error to 50%.

According to Fig. 9, the first-order slip velocity model defined in the previous section shows more accurate results in the whole range of the studied Knudsen numbers in comparison to the bare diffusive boundary condition. A good agreement between LB and DSMC results is observed for Knudsen numbers equal to or smaller than 0.1 (error less than 5%). Using more grid points can make the slip velocity prediction even more accurate. Nevertheless, the accuracy of the slip velocity model drops when Kn is larger than 0.2 and the channel height is discretized with reduced grid points (=10). It is noted that the deviation appearing at higher Knudsen numbers is due to the inaccuracy of the first-order Maxwell model as discussed in Dongari *et al.* [67]. It is worth noting that Knudsen numbers up to 0.1, for which the developed model shows good performance, cover most practical microflow devices.

The present results demonstrate that with a correct slip velocity, the diffusive boundary condition can be used in the slip flow regime with reduced grid points. This finding can play a pivotal role in 3D numerical simulations of complex geometries such as porous media where grid refinement in all channels (pores) is practically impossible. Therefore, the results show that the slip velocity model with diffusive boundary condition can be utilized for very narrow and finely discretized pores and channels leading to more efficient and inexpensive simulations. For higher Knudsen numbers (Kn > 0.2), the Knudsen layer should be taken into account in the slip velocity model by incorporating the second derivative of velocity at the solid wall as discussed in [24–26,65]. Finally, the results discussed in this section are generally independent of the relaxation time. The range of relaxation times in the present simulations varies by two orders of magnitude [$O(0.01)$ to $O(1)$].

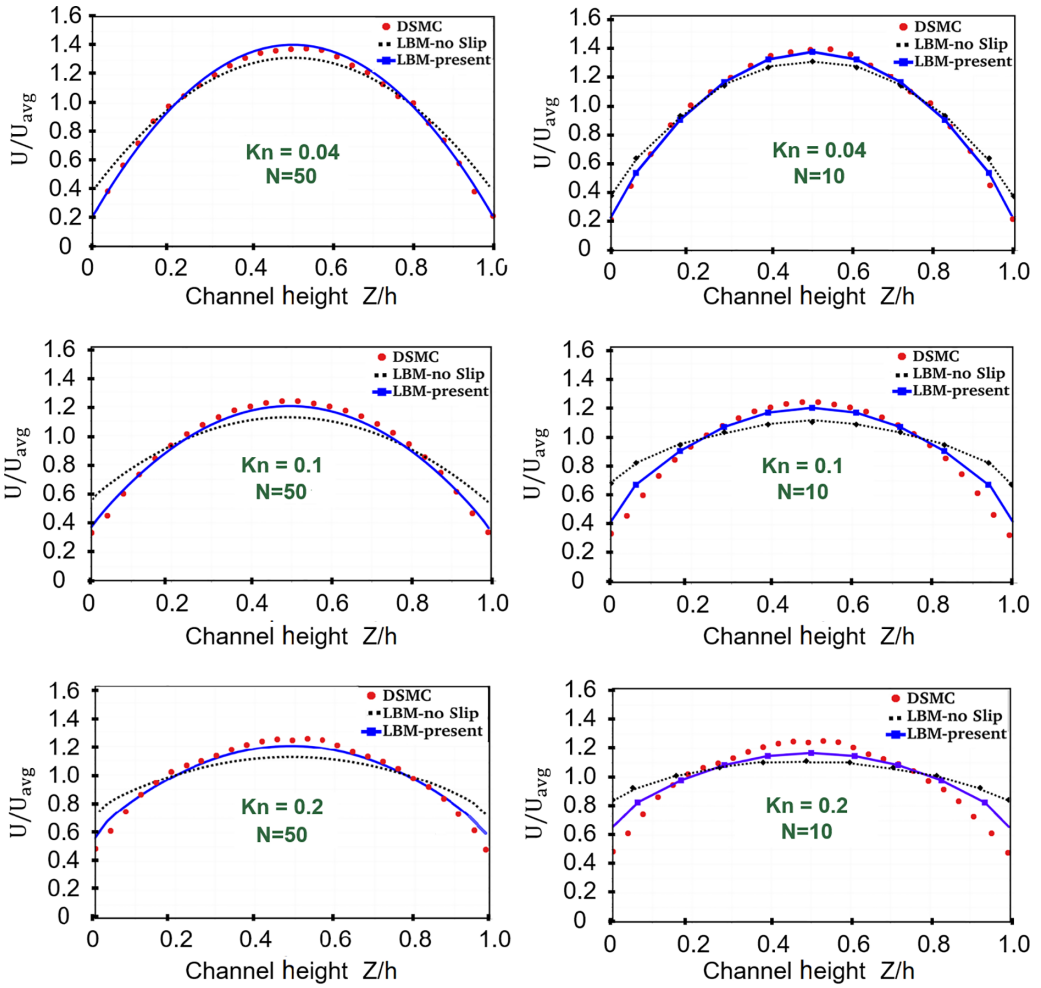

FIG. 9. Effect of Knudsen number and grid refinement (transverse grid points N) on the velocity profile across a nonreactive channel: DSMC (filled circles) [23], bare diffusive boundary condition (dashed lines), and the present model (solid lines).

C. Velocity and concentration slips impact on catalytic reaction rate

In this section, the model presented in Sec. IV is employed to study the effect of key parameters such as temperature jump, surface Damköhler number, Knudsen number, and mass accommodation coefficient on the catalytic reaction rate. It is known that these parameters play an important role when a concentration jump changes the reaction rate at the catalytic wall. In spite of a broad consensus on the negligible effect of velocity slip on the reaction rate, there is a debate regarding the importance of other parameters. While Xu and Ju [34] reported that the concentration jump can increase the reaction rate if the species Damköhler number is large, Zade *et al.* [36] did not observe a noticeable change due to the concentration jump. They even reported that the concentration jump may reduce the reaction rate if the temperature jump ($\sqrt{\frac{T_w}{T_s}}$) is included in the concentration jump as well. Furthermore, Xu and Ju [34] showed numerically that a mass accommodation coefficient of 0.1 changes the reaction rate noticeably for high surface Damköhler numbers ($\mathrm{Da}_s > 1.0$). Conversely, Zade *et al.* [36] reported that the mass accommodation has little impact on the concentration jump and reaction rate. In contrast to the results published in Ref. [36], where only a catalytic reaction is considered, Xu and Ju [34] considered both heterogeneous (catalytic) and homogeneous (gas-phase) reactions in their simulations.

A numerical simulation for the biogas methanation reaction is performed with 17% carbon monoxide and 83% hydrogen (per volume) at the inlet. In all simulations, $\mathrm{Kn}_d = 0.11$ at the inlet, since it has been shown that the effect of concentration jump is unimportant for smaller Kn numbers [2,34–36]. The inlet and wall temperatures are fixed at 1200 K. The effect of concentration jump introduced via Eq. (32) is taken into account, and the results are compared against the bare model without concentration jump. Since the channel height is very small, the Peclet number decreases appreciably and the reactant is consumed quickly near the inlet. To compensate for the decrease in channel height (similar to Xu and Ju [34]), the inlet velocity is increased to 60 m/s, an order of magnitude higher than the previous simulations. Two surface Damköhler numbers, 0.1 and 1.0, are considered. CO is the deficient reactant, and the reaction rate is described as a function of CO concentration as in Sec. III A. All other parameters discussed here are calculated for the deficient CO reactant.

According to Eq. (32), the term $\mathrm{Da}_{ds}\mathrm{Kn}_d A_2$ may influence the reaction rate only if it is comparable to the other terms in

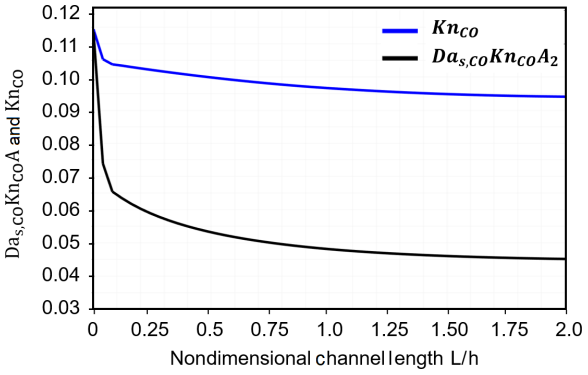

FIG. 10. Variation of $\mathrm{Kn_{CO}}$ and $\mathrm{Da_{CO}Kn_{CO}}A_2$ at the reactive wall along the channel ($A_2 = 1.0$).

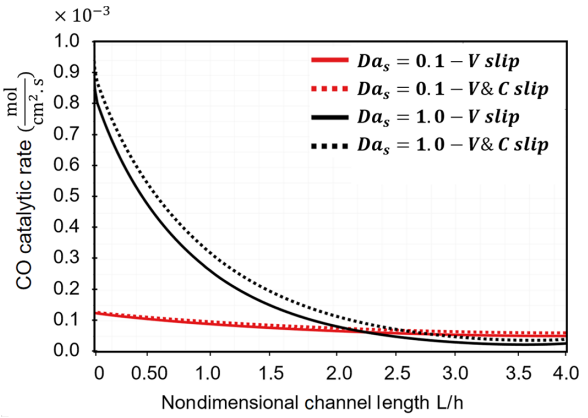

FIG. 11. Effect of velocity and concentration slips on the local catalytic CO conversion rate along the channel at two Damköhler numbers (0.1 and 1.0).

the denominator. The first observation is that the temperature jump ($\sqrt{\frac{T_w}{T_s}}$) has a negative effect on the reaction rate. It should be noted that this effect is different from the temperature jump, which has a direct impact on the reaction rate through the reaction rate coefficient k. In the presence of a temperature jump contribution in the concentration jump, the reaction rate calculated from Eq. (32) decreases—provided that the wall temperature is higher than the inlet temperature (which is typically the case in most practical catalytic systems). This theoretical prediction supports the results published by Zade *et al.* [36]. Contrary to Xu and Ju [34], Zade *et al.* adjusted $\sqrt{\frac{T_w}{T_s}} = 1.0$ artificially to evaluate independently the impact of the temperature jump on the reaction rate. This simulation condition may clarify the differences between these two studies, although further investigation is still required to understand the underlying physical reasons for the observed differences. Since the present simulations are isothermal, it is not possible to investigate the effect of temperature jump numerically. Therefore, this effect is not further elaborated.

In many practical applications, the properties of the mixture are assumed to be constant. However, nondimensional numbers such as Da_s and Kn can alter due to the change in mixture composition. Figure 10 shows the variation of Kn_d and $\mathrm{Da}_{ds}\mathrm{Kn}_d A_2$ numbers for the deficient reactant CO along the channel when $A_2 = 1.0$ and the surface Damköhler number at the inlet is 1.0. The local values show a small change in Knudsen number, while $\mathrm{Da}_{ds}\mathrm{Kn}_d A_2$ drops more than 50%. This can be one reason for the reducing impact of concentration jump with increasing axial distance. It is worth noting that Kn and Da_s numbers for other species can either increase or decrease along the channel; herein, only the deficient species is evaluated since it has a direct impact on the reaction rate.

The catalytic reaction rate of the deficient CO reactant along the channel is plotted in Fig. 11. The mass accommodation coefficient is the same in all simulations, and the impact of surface Damköhler number on concentration jump and reaction rate is exposed. All simulations include the slip velocity boundary condition for two reasons. First, the diffusive boundary condition produces slip velocity even without a slip velocity model, as discussed earlier. Second, it was shown that the effect of slip velocity on concentration and reaction rate is negligible [2,35]. Therefore, the velocity slip and no-slip conditions result in a very similar concentration distribution in the channel.

The surface Damköhler number should be high enough in practical systems so as to promote high reaction rates at the wall and hence high reactant conversions at a given channel length. In fact, concentration jump cannot improve the reaction rate at low Da_s numbers. The reaction rate increases by about 10% in comparison to simulations without concentration jump for $\mathrm{Da}_s = 1.0$. The obtained results may answer the apparent contradiction reported by Zade *et al.* [36] and Xu and Ju [34]. Simulations by Zade *et al.* [36], indicating that the effect of concentration jump without the effect of temperature jump is negligible, were performed at a relatively low surface Damköhler number; Xu and Ju [34], however, conducted their simulations at high surface Damköhler numbers up to 10. For this reason, the specific effect of concentration jump was not obvious in earlier simulations.

Equation (32) provides a good estimate of the effects of key parameters on the reaction rate. This explicit relation has a great advantage over previous implicit models where desired dependencies were implied through simulation results and not theoretically. Four different cases are compared in Fig. 12. The effect of concentration jump is incorporated through Eq. (32), but the surface Damköhler number and mass accommodation coefficients are different. A surface accommodation coefficient of unity implies that all molecules hitting the surface reach thermodynamic equilibrium whereas smaller values denote that a lower percentage of molecules equilibrate after impinging at the surface and the rest are reflected specularly back into the flow without reaching thermodynamic equilibrium. The mass accommodation coefficient plays almost no role in the reaction rate when other parameters such as Da_s and Kn are small. On the other side, its influence can be even higher than that of the surface Damköhler number when $\mathrm{Da}_s \gg 0.1$. The main reason is that the Damköhler number increases through the reaction coefficient k which appears in the denominator of Eq. (32). Therefore, both $\mathrm{Da}_{ds}\mathrm{Kn}_d A_2$ and $\frac{k}{D_{md}}$ increase at the same time, and the effect of the Damköhler number is not that significant. On the other hand, the term $\alpha_{m,j}$ increases $\mathrm{Da}_{ds}\mathrm{Kn}_d A_2$ without altering the second term

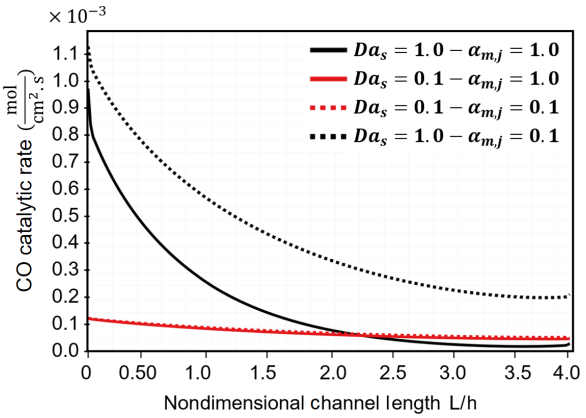

FIG. 12. Effect of mass accommodation factor $\alpha_{m,j}$ on the local catalytic CO conversion along the channel at two surface Damköhler numbers (0.1 and 1.0).

in the denominator. Consequently, the impact of the mass accommodation becomes more significant.

Regarding the concentration jump, we adopted an available theory from Ref. [34] and developed the boundary condition in LB for the concentration jump according to Eq. (32). To the best of our understanding, there is no solid theory for a second-order concentration jump model. Xu and Ju [34] used also a similar first-order concentration jump for even higher Damköhler numbers (up to 10) than those in our paper. The developed model with velocity slips and concentration jumps is of particular interest for many microflows, such as those encountered in catalytic microthrusters for space applications (used for the steering of small satellites, etc.). Therein, the operating pressure is in the millibar range, leading to appreciable Knudsen numbers [73,74].

VI. CONCLUSIONS

A consistent boundary condition for both equimolar and nonequimolar catalytic isothermal reactions was developed, further accounting for the effects of velocity slips and concentration jumps. The developed model incorporates the diffusion coefficients of all species in the calculation of the catalytic reaction rate as well as the correct velocity at the catalytic reactive boundary node. As a test case, the biogas methanation reaction is simulated using both LB and conventional CFD methods in a channel-flow geometry. A good agreement was achieved between LB and CFD results in terms of flow velocities and densities as well as in species distributions.

The inclusion of velocity slips and concentration jumps on the catalytic reaction is studied. The velocity slip model was first compared to DSMC results from the literature for nonreactive cases at three different Knudsen numbers (0.04, 0.1, and 0.2). The results indicate that the slip model based on the first-order velocity derivative can predict the slip velocity quite accurately. However, the accuracy deteriorates as the Knudsen number increases (higher than 0.1) and/or fewer grids ($N < 10$) are used across the channel/pore. Lastly, the proposed models are applied to evaluate the effect of concentration jump on the catalytic reaction. Theoretical and numerical results show that the term $\mathrm{Da}_{ds}\mathrm{Kn}_d A_2$ (with d denoting the deficient species in the reaction) determines the significance of the concentration jump on the reaction rate. The effect of temperature jump on concentration jump and reaction rate is finally discussed. The developed catalytic model with velocity slip and concentration jump effects is of interest in many practical microflow systems, such as catalytic microthrusters for space applications, operating at pressures of a few millibar and hence at Knudsen numbers in the slip flow regime.

ACKNOWLEDGMENTS

We acknowledge support from the Swiss National Science Foundation (SNSF) under Project No. 200021_179019, the Swiss Federal Office of Energy (SFOE) under Project No. SI/501976-01, and the Swiss Supercomputing Center CSCS under projects s1082, psi03, and s1010.

APPENDIX: DISCRETIZED BOLTZMANN EQUATION

Equation (1) is a discrete-velocity kinetic equation. The lattice Boltzmann equation obtained by time discretization using the trapezoidal rule can be derived as follows (for details, see [51]):

$$g_{ji}(t+\delta t) = g_{ji}(t) - \frac{2\delta t}{\delta t + 2\tau_{j1}}[g_{ji}(t) - f^{*}_{ji}(t)] - \frac{2\delta t}{\delta t + 2\tau_{j1}}\frac{\tau_{j1}}{\tau_{j2}}\left[f^{*}_{ji}(t) - f^{\mathrm{eq}}_{ji}(t)\right] + \frac{2\tau_{j1}\delta t}{\delta t + 2\tau_{j1}}[\Psi_{ji}(t)], \tag{A1}$$

where g_{ji} is the transformation population [51]. The local species density and momentum are functions of the populations g_{ji} as follows:

$$\rho_j(f) = \rho_j(g), \tag{A2}$$

$$J_{j\alpha}(f) = \frac{J_{j\alpha}(g) + \frac{\delta t}{2\tau_{j2}}J^{\mathrm{eq}}_{j\alpha}(f) + \frac{\delta t}{2}\sum_{i=0}^{26} c_{ji\alpha}\Psi_{ji}}{1 + \frac{\delta t}{2\tau_{j2}}}. \tag{A3}$$

Therefore, the correction term Ψ_{ji} appears not only in the lattice Boltzmann equation [Eq. (A1)], but also in the momentum $J_{i\alpha}$.

[1] S. Succi, Mesoscopic Modeling of Slip Motion at Fluid-Solid Interfaces with Heterogeneous Catalysis, Phys. Rev. Lett. **89**, 064502 (2002).

[2] A. Q. Zade, M. Renksizbulut, and J. Friedman, Slip/jump boundary conditions for rarefied reacting/non-reacting multicomponent gaseous flows, Int. J. Heat Mass Transf. **51**, 5063 (2008).

[3] W. M. Zhang, G. Meng, and X. Wei, A review on slip models for gas microflows, Microfluid. Nanofluid. **13**, 845 (2012).

[4] T. Krüger, H. Kusumaatmaja, A. Kuzmin, O. Shardt, G. Silva, and E. M. Viggen, *The Lattice Boltzmann Method* (Springer International, 2017), Vol. 10, pp. 4–15.

[5] N. I. Prasianakis, T. Rosén, J. Kang, J. Eller, J. Mantzaras, and F. N. Büchi, Simulation of 3D porous media flows with application to polymer electrolyte fuel cells, Commun. Computat. Phys. **13**, 851 (2013).

[6] I. Ginzburg, Lattice Boltzmann modeling with discontinuous collision components: Hydrodynamic and advection-diffusion equations, J. Stat. Phys. **126**, 157 (2007).

[7] I. Ginzburg, F. Verhaeghe, and D. d'Humìeres, Two-relaxation-time lattice Boltzmann scheme: about parametrization, velocity, pressure and mixed boundary conditions, Commun. Computat. Phys. **3**, 427 (2008).

[8] T. Reis and P. J. Dellar, Lattice Boltzmann simulations of pressure-driven flows in microchannels using Navier-Maxwell slip boundary conditions, Phys. Fluids **24**, 112001 (2012).

[9] Z. Guo and C. Zheng, Analysis of lattice Boltzmann equation for microscale gas ows: relaxation times, boundary conditions and the knudsen layer, International Journal of Computational Fluid Dynamics **22**, 465 (2003).

[10] M. A. Safi, N. I. Prasianakis, J. Mantzaras, A. Lamibrac, and F. N. Büchi, Experimental and pore-level numerical investigation of water evaporation in gas diffusion layers of polymer electrolyte fuel cells, Int. J. Heat Mass Transf. **115**, 238 (2017).

[11] M. A. Safi, J. Mantzaras, N. I. Prasianakis, A. Lamibrac, and F. N. Büchi, A pore-level direct numerical investigation of water evaporation characteristics under air and hydrogen in the gas diffusion layers of polymer electrolyte fuel cells, Int. J. Heat Mass Transf. **129**, 1250 (2019).

[12] M. Khatoonabadi, M. A. Safi, N. I. Prasianakis, J. Roth, J. Mantzaras, and N. Kirov, F. N. Büchi, Insights on the interaction of serpentine channels and gas diffusion layer in an operating polymer electrolyte fuel cell: Numerical modeling across scales, Int. J. Heat Mass Transf. **181**, 121859 (2021).

[13] Z. Chai, Z. Guo, L. Zheng, B. Shi, Lattice Boltzmann simulation of surface roughness effect on gaseous flow in a microchannel, J. Appl. Phys. **104**, 014902 (2008).

[14] N. Prasianakis and S. Ansumali, Microflow simulations via the lattice Boltzmann method, Commun. Computat. Phys. **9**, 1128 (2011).

[15] J. Meng, X. J. Gu, and D. R. Emerson, Analysis of non-physical slip velocity in lattice Boltzmann simulations using the bounce-back scheme, J. Computat. Sci. **28**, 476 (2018).

[16] G.-H. Tang, Y.-H. Zhang, and D. R. Emerson, Lattice Boltzmann models for nonequilibrium gas flows, Phys. Rev. E **77**, 046701 (2008).

[17] C. R. Lilley and J. E. Sader, Velocity profile in the Knudsen layer according to the Boltzmann equation, Proc. R. Soc. A **464**, 2015 (2008).

[18] M. Nourmohammadzadeh, M. Rahnama, S. Jafari, and A. Akhgar, Microchannel flow simulation in transition regime using lattice Boltzmann method, Proc. Inst. Mech. Eng., Part C **226**, 552 (2012).

[19] D. K. Bhattacharya and G. C. Lie, Molecular-Dynamics Simulations of Nonequilibrium Heat and Momentum Transport in Very Dilute Gases, Phys. Rev. Lett. **62**, 897 (1989).

[20] D. L. Morris, L. Hannon, and A. L. Garcia, Slip length in a dilute gas, Phys. Rev. A **46**, 5279 (1992).

[21] J. C. Maxwell, On stresses in rarified gases arising from inequalities of temperature, Philos. Trans. R. Soc. London **170**, 231 (1879).

[22] I. V. Karlin and S. Ansumali, Renormalization of the lattice Boltzmann hierarchy, Phys. Rev. E **76**, 025701(R) (2007).

[23] S. H. Kim, H. Pitsch, and I. D. Boyd, Accuracy of higher-order lattice Boltzmann methods for microscale flows with finite Knudsen numbers, J. Comput. Phys. **227**, 8655 (2008).

[24] W. P. Yudistiawan, S. Ansumali, and I. V. Karlin, Hydrodynamics beyond Navier-Stokes: The slip flow model, Phys. Rev. E **78**, 016705 (2008).

[25] A. C. Sousa, M. Hadavand, and A. Nabovati, Three-dimensional simulation of slip-flow and heat transfer in a microchannel using the lattice Boltzmann method, WIT Trans. Eng. Sci. **68**, 75 (2010).

[26] S. Bennett, P. Asinari, and P. J. Dellar, A lattice Boltzmann model for diffusion of binary gas mixtures that includes diffusion slip, Int. J. Numer. Methods Fluids **69**, 171 (2012).

[27] X. J. Gu, D. R. Emerson, and G. H. Tang, Kramers' problem and the Knudsen minimum: A theoretical analysis using a linearized 26-moment approach, Contin. Mech. Thermodyn. **21**, 345 (2009).

[28] J. Meng and Y. Zhang, Diffuse reflection boundary condition for high-order lattice Boltzmann models with streaming-collision mechanism, J. Comput. Phys. **258**, 601 (2014).

[29] Z. Chai, B. Shi, Z. Guo, J. Lu, Gas flow through square arrays of circular cylinders with klinkenberg effect: A lattice boltzmann study, Commun. Comput. Phys. **8**, 1052 (2010).

[30] C. D. Scott, Wall boundary equations with slip and catalysis for multicomponent, nonequilibrium gas flows, Technical Report NASA TM X-58111 (1973).

[31] R. N. Gupta, C. D. Scott, and J. N. Moss, Slip-boundary equations for multicomponent nonequilibrium airflow, Technical Report NASA TM 85820 (1985).

[32] G. A. Bird, *Molecular Gas Dynamics and the Direct Simulation of Gas Flows* (Oxford University Press, Oxford, UK, 1994).

[33] D. E. Rosner and D. H. Papadopoulos, Jump, slip, and creep boundary conditions at nonequilibrium gas/solid interfaces, Ind. Eng. Chem. Res. **35**, 3210 (1996).

[34] B. Xu and Y. Ju, Theoretical and numerical studies of non-equilibrium slip effects on a catalytic surface, Combust. Theor. Model. **10**, 961 (2006).

[35] B. Xu and Y. Ju, Concentration slip and its impact on heterogeneous combustion in a micro scale chemical reactor, Chem. Eng. Sci. **60**, 3561 (2005).

[36] A. Q. Zade, M. Renksizbulut, and J. Friedman, Rarefaction effects on the catalytic oxidation of hydrogen in microchannels, Chem. Eng. J. **181-182**, 643 (2012).

[37] F. J. Alexander, H. Chen, S. Chen, and G. D. Doolen, Lattice Boltzmann model for compressible fluids, Phys. Rev. A **46**, 1967 (1992).

[38] Z.-H. Chai and T.-S. Zhao, A pseudopotential-based multiple-relaxation-time lattice Boltzmann model for multicomponent/multiphase flows, Acta Mech. Sin. **28**, 983 (2012).

[39] N. Looije, J. J. J. Gillissen, S. Sundaresan, and H. E. A. Van Den Akker, Introducing a variable speed of sound in single-component lattice Boltzmann simulations of isothermal fluid flows, Comput. Fluids **167**, 129 (2018).

[40] H. E. Van den Akker, R. Donkers, G. T. Zachariah, and O. Shardt, On using variable molecular masses in multicomponent

lattice Boltzmann simulations, J. Computat. Sci. **54**, 101432 (2021).
[41] H. Yu and K. Zhao, Lattice Boltzmann method for compressible flows with high mach numbers, Phys. Rev. E **61**, 3867 (2000).
[42] J. M. Buick and J. A. Cosgrove, Investigation of a lattice Boltzmann model with a variable speed of sound, J. Phys. A **39**, 13807 (2006).
[43] L. Vienne, S. Marié, and F. Grasso, Lattice Boltzmann method for miscible gases: A forcing-term approach, Phys. Rev. E **100**, 023309 (2019).
[44] S. Arcidiacono, I. V. Karlin, J. Mantzaras, and C. E. Frouzakis, Lattice Boltzmann model for the simulation of multicomponent mixtures, Phys. Rev. E **76**, 046703 (2007).
[45] A. Bardow, I. V. Karlin, and A. A. Gusev, Multispeed models in off-lattice Boltzmann simulations, Phys. Rev. E **77**, 025701(R) (2008).
[46] S. Agrawal, S. Singh, and S. Ansumali, Fokker-Planck model for binary mixtures, J. Fluid Mech. **899**, A25 (2020).
[47] N. Sawant, B. Dorschner, and I. V. Karlin, Consistent lattice Boltzmann model for multicomponent mixtures, J. Fluid Mech. **909**, A1 (2021).
[48] N. Sawant, B. Dorschner, and I. Karlin, A lattice Boltzmann model for reactive mixtures, Philos. Trans. R. Soc., A **379**, 20200402 (2021).
[49] N. Sawant, B. Dorschner, and I. V. Karlin, Consistent lattice Boltzmann model for reactive mixtures, J. Fluid Mech. **941**, A62 (2022).
[50] S. Arcidiacono, J. Mantzaras, and I. V. Karlin, Lattice Boltzmann simulation of catalytic reactions, Phys. Rev. E **78**, 046711 (2008).
[51] J. Kang, N. I. Prasianakis, and J. Mantzaras, Thermal multicomponent lattice Boltzmann model for catalytic reactive flows, Phys. Rev. E **89**, 063310 (2014).
[52] N. Kulyk, D. Berger, A. S. Smith, and J. Harting, Catalytic flow with a coupled finite difference–Lattice Boltzmann scheme, Comput. Phys. Commun. **256**, 107443 (2020).
[53] M. Khatoonabadi, N. I. Prasianakis, and J. Mantzaras, Lattice Boltzmann model with generalized wall boundary conditions for arbitrary catalytic reactivity, Phys. Rev. E **103**, 063303 (2021).
[54] S. Arcidiacono, S. Ansumali, I. V. Karlin, J. Mantzaras, and K. B. Boulouchos, Entropic lattice Boltzmann method for simulation of binary mixtures, Math. Comput. Simul. **72**, 79 (2006).
[55] C. R. Wilke, A viscosity equation for gas mixtures, J. Chem. Phys. **18**, 517 (1950).
[56] W. Bird, R. B. Stewart, and E. Lightfoot, *Transport Phenomena*, 2nd ed. (John Wiley and Sons, Inc., New York, 2007).
[57] Z. Chai, X. Guo, L. Wang, and B. Shi, Maxwell-Stefan-theory-based lattice Boltzmann model for diffusion in multicomponent mixtures, Phys. Rev. E **99**, 023312 (2019).
[58] R. Sui, J. Mantzaras, and R. Bombach, H_2 and CO heterogeneous kinetic coupling during combustion of $H_2/CO/O_2/N_2$ mixtures over rhodium, Combustion and Flame **202**, 292 (2019).
[59] R. J. Kee, G. Dixon-Lewis, J. Warnatz, M. E. Coltrin, and J. A. Miller, A Fortran Computer Code Package for the Evaluation of Gas-phase Multicomponent Transport Properties, Technical Report SAND86-8246, Sandia National Laboratories (1986).
[60] K. Sutton and P. Gnoffo, Multi-component diffusion with application to computational aerothermodynamics, in *7th AIAA/ASME Joint Thermophysics and Heat Transfer Conference, Albuquerque, NM, USA*, Vol. AIAA 98-2575 (AIAA, 1998).
[61] R. J. Kee, F. M. Rupley, E. Meeks, and J. A. Miller, CHEMKIN-III: A FORTRAN chemical kinetics package for the analysis of gas-phase chemical and plasma kinetics, Technical Report SAND96-8216, Sandia National Laboratories (1996).
[62] H. Grad, On the kinetic theory of rarefied gases, Commun. Pure Appl. Math. **2**, 331 (1949).
[63] M. Reinke, J. Mantzaras, R. Schaeren, R. Bombach, A. Inauen, and S. Schenker, High-pressure catalytic combustion of methane over platinum: In situ experiments and detailed numerical predictions, Combust. Flame **136**, 217 (2004).
[64] J. Mantzaras, R. Sui, C. K. Law, and R. Bombach, Heterogeneous and homogeneous combustion of fuel-lean $C_3H_8/O_2/N_2$ mixtures over rhodium at pressures up to 6 bar, Proc. Combust. Inst. **38**, 6473 (2020).
[65] G. Silva and V. Semiao, Consistent lattice Boltzmann modeling of low-speed isothermal flows at finite Knudsen numbers in slip-flow regime: Application to plane boundaries, Phys. Rev. E **96**, 013311 (2017).
[66] G. Karniadakis, A. Beskok, and N. Aluru, *Microflows and Nanoflows: Fundamentals and Simulation*, 1st ed., Vol. 29 (Springer, New York, NY, 2006).
[67] N. Dongari, A. Agrawal, and A. Agrawal, Analytical solution of gaseous slip flow in long microchannels, Int. J. Heat Mass Transf. **50**, 3411 (2007).
[68] H. C. Weng and C.-K. Chen, A challenge in Navier-Stokes-based continuum modeling: Maxwell-Burnett slip law, Phys. Fluids **20**, 106101 (2008).
[69] G. Silva, Consistent lattice Boltzmann modeling of low-speed isothermal flows at finite Knudsen numbers in slip-flow regime. II. Application to curved boundaries, Phys. Rev. E **98**, 023302 (2018).
[70] J. Kopyscinski, T. J. Schildhauer, F. Vogel, S. M. Biollaz, and A. Wokaun, Applying spatially resolved concentration and temperature measurements in a catalytic plate reactor for the kinetic study of CO methanation, J. Catal. **271**, 262 (2010).
[71] Q. Zou and X. He, On pressure and velocity boundary conditions for the lattice Boltzmann BGK model, Phys. Fluids **9**, 1591 (1997).
[72] Y. Ghermay, J. Mantzaras, and R. Bombach, Effects of hydrogen preconversion on the homogeneous ignition of fuel-lean $H_2/O_2/N_2/CO_2$ mixtures over platinum at moderate pressures, Combust. Flame **157**, 1942 (2010).
[73] G. A. Boyarko, C.-J. Sung, and S. J. Schneider, Catalyzed combustion of hydrogen–oxygen in platinum tubes for micro-propulsion applications, Proc. Combust. Inst. **30**, 2481 (2005).
[74] S. J. Volchko, C.-J. Sung, Y. Huang, and S. J. Schneider, Catalytic combustion of rich methane/oxygen mixtures for micropropulsion applications, J. Propul. Power **22**, 684 (2006).